

## THE DISTRIBUTION AND EXCITATION OF CH<sub>3</sub>CN IN A SOLAR NEBULA ANALOG

RYAN A. LOOMIS<sup>1,2</sup>, L. ILSEDORE CLEEVE<sup>2</sup>, KARIN I. ÖBERG<sup>2</sup>, AND COLLABORATORS

*Draft version October 3, 2017*

### ABSTRACT

We have detected and spatially resolved seven transitions of CH<sub>3</sub>CN toward the disk surrounding the T-Tauri star TW Hya. Using a rotational diagram analysis we find a disk-averaged column density of  $N_T = 1.82_{-0.19}^{+0.25} \times 10^{12}$  cm<sup>-2</sup> and a rotational temperature of  $T_{rot} = 29.3_{-2.8}^{+3.2}$  K. A radially resolved rotational diagram shows the rotational temperature to be roughly constant across the disk, suggesting that the CH<sub>3</sub>CN emission originates from a vertically banded layer in the disk at  $z/r \sim 0.3$ . Through comparison of the observations with predictions from a disk chemistry model, we find that grain-surface reactions likely dominate CH<sub>3</sub>CN formation and that *in situ* disk chemistry is sufficient to explain CH<sub>3</sub>CN abundances without invoking inheritance from the protostellar phase. We discuss the ramifications of these results for exocometary compositions and compare the CH<sub>3</sub>CN(gr)/H<sub>2</sub>O(gr) ratio predicted by our model to measured Solar System cometary values.

### 1. INTRODUCTION

Observations of comets and meteorites, which are thought to pristinely trace the material they formed from, show that the planet and comet forming midplane of the young Solar Nebula had a rich organic volatile composition (e.g., Mumma & Charnley 2011). In particular, ALMA observations and the Rosetta mission have both recently shown that comets are abundant in nitrile species such as HCN and CH<sub>3</sub>CN (e.g., Cordiner et al. 2014; Le Roy et al. 2015). Tracing the chemistry of this family of organic molecules is of special interest, as HCN and related nitriles are the starting point for the synthesis of most important bio-molecules (e.g., Bernstein et al. 2002; Powne et al. 2009; Powne et al. 2010; Patel et al. 2015).

In the protoplanetary disks where other planetary systems are just starting to form, the smallest nitriles CN and HCN have long been well-known (e.g., Dutrey et al. 1997; van Zadelhoff et al. 2001), but larger nitriles such as HC<sub>3</sub>N have only been found more recently (Chapillon et al. 2012), and ALMA is just now beginning to reveal more complex species such as CH<sub>3</sub>CN (Öberg et al. 2015). What remains unknown, however, is whether these nitriles are directly inherited from the chemically rich protostellar stage (e.g., Jørgensen et al. 2016), or if they are destroyed as material accretes onto the disk (e.g., Sakai et al. 2014) and then reformed *in situ* (e.g., Walsh et al. 2014). If the latter is true, the unique properties of each disk likely play a large role in setting the nitrile content of their forming planetesimals and comets.

Testing the origin of nitriles such as CH<sub>3</sub>CN in disks requires constraining both their formation chemistry and distribution. CH<sub>3</sub>CN can efficiently form through both gas-phase and grain-surface reactions, and observational constraints have thus far been limited to a single source (Öberg et al. 2015). Öberg et al. (2015) interpreted these observations to suggest that CH<sub>3</sub>CN forms efficiently on grain-surfaces and is then UV photodesorbed into the

gas-phase. Dominant formation through grain-surface reactions has significant ramifications for the midplane abundance of CH<sub>3</sub>CN, and therefore the final composition of forming planets and comets. Better constraints on the distribution and excitation of CH<sub>3</sub>CN in disks to confirm this hypothesis are therefore crucial to connect disk chemistry to cometary measurements.

In this paper we present the detection of seven lines of CH<sub>3</sub>CN in the disk around TW Hya. A well-studied old (5–15 Myr) T Tauri star, TW Hya hosts the closest ( $59.5 \pm 1$  pc) protoplanetary disk, and is a good analog for the Solar Nebula ( $0.8 M_\odot$ , spectral type K7, e.g., Kastner et al. 1997; Qi et al. 2004, 2006; Andrews et al. 2012; Bergin et al. 2013; Andrews et al. 2016). We present the observations and the details of their reduction and imaging in §2. As the upper state energies of the observed transitions span a wide range ( $\sim 70$ – $150$ K), we are able to use a rotational diagram analysis to empirically constrain the CH<sub>3</sub>CN column density and rotational temperature. Results of both disk-averaged and radially resolved analyses are presented in §3, along with a comparison to predictions from detailed chemical models. In §4 we discuss these results and their implications for midplane CH<sub>3</sub>CN abundances and incorporation into planetesimals and forming comets. A summary is given in §5.

### 2. OBSERVATIONS

#### 2.1. Observational details

TW Hya was observed on 29-Dec-2016 and 09-Jan-2017 in Band 6 as part of the ALMA Cycle 4 project 2016.1.01046.S. The first execution block included 43 antennas with projected baseline lengths between 15 and 460 m (11–353 kλ). The second execution block included 47 antennas with projected baseline lengths between 15 and 384 m (11–295 kλ). The on-source integration times were 32 and 31 minutes, respectively, for a total on-source integration time of 63 minutes. The correlator setup was identical for both execution blocks and included a Time Division Mode (TDM) continuum window centered at 237 GHz with a bandwidth of 2 GHz as well as Frequency Division Mode (FDM) spectral windows centered

<sup>1</sup> Corresponding author: rloomis@cfa.harvard.edu

<sup>2</sup> Harvard-Smithsonian Center for Astrophysics, Cambridge, MA 02138

**Table 1**  
Observed spectral lines

MWC 480					
Transition	Frequency (MHz)	E <sub>u</sub> (K)	S <sub>ij</sub> μ <sup>2</sup> (D <sup>2</sup> )	Int. Flux Dens. (mJy km s <sup>-1</sup> )	Filter response (σ)
12 <sub>0</sub> –11 <sub>0</sub>	220747.3 <sup>a</sup>	68.9	183.7 <sup>b</sup>	82 ± 7	17.8
12 <sub>1</sub> –11 <sub>1</sub>	220743.0 <sup>a</sup>	76.0	182.5 <sup>b</sup>	78 ± 7	15.9
12 <sub>2</sub> –11 <sub>2</sub>	220730.3 <sup>a</sup>	97.4	178.6 <sup>b</sup>	41 ± 7	7.2
13 <sub>0</sub> –12 <sub>0</sub>	239137.9 <sup>a</sup>	80.3	199.1 <sup>b</sup>	81 ± 7	13.1
13 <sub>1</sub> –12 <sub>1</sub>	239133.3 <sup>a</sup>	87.5	197.9 <sup>b</sup>	70 ± 7	9.3
13 <sub>2</sub> –12 <sub>2</sub>	239119.5 <sup>a</sup>	108.9	194.3 <sup>b</sup>	28 ± 7	5.7
13 <sub>3</sub> –12 <sub>3</sub>	239096.5 <sup>a</sup>	144.6	188.5 <sup>b</sup>	12 ± 7	3.5

<sup>a</sup> Center frequency of collapsed hyperfine components (spacing smaller than channel width).

<sup>b</sup> S<sub>ij</sub>μ<sup>2</sup> of combined hyperfine components.

at 219.560, 220.740, and 239.112 GHz. These spectral windows had bandwidths of 58.59 MHz and channel spacings of 61 kHz ( $\sim 0.08$  km s<sup>-1</sup>), and they targeted the C<sup>18</sup>O J=2–1, CH<sub>3</sub>CN J=12–11, and CH<sub>3</sub>CN J=13–12 molecular transitions, respectively.

For both executions, the quasar J1058+1033 was used for bandpass calibration and the quasar J1037-2934 was used for phase calibration. Callisto was used as the flux calibrator for the first execution, and Ganymede was used as the flux calibrator for the second execution. We additionally used the disk continuum emission in each execution block to perform three rounds of phase self-calibration and one round of amplitude self-calibration in CASA version 4.3.

## 2.2. Results

The observations were first analyzed using a matched filtering technique described in Loomis et al. (subm.). The C<sup>18</sup>O J=2–1 transition was imaged using CLEAN at the native spectral resolution (61 kHz,  $\sim 0.08$  km s<sup>-1</sup>) with Briggs weighting (robust=0.5), producing a high SNR image cube. This image cube was then used as a filter for the CH<sub>3</sub>CN spectral windows using the VISIBLE code<sup>3</sup>. From the resultant filter impulse response spectra, we detected all three transitions in the J=12–11 k-ladder with spectral coverage and all four transitions in the J=13–12 k-ladder with spectral coverage. These transitions are tabulated in Table 1, along with the peak filter responses for each transition.

These seven transitions were then individually imaged using CLEAN with natural weighting and a velocity resolution of 0.2 km s<sup>-1</sup>, centering each image cube on the transition rest frequency. The J=13–12 transitions had a small uv-taper ('outertaper' = 0''.35) applied to force the synthesized beam to match that of the J=12–11 transitions (1''.05 × 0''.83). The rms of the image cubes was  $\sim 3.2$  mJy bm<sup>-1</sup> in each channel, and channel maps are presented in Appendix A. Moment-0 maps of the transitions are shown in Fig. 1 and were created by integrating all emission between 2.1–3.7 km s<sup>-1</sup> with no clipping threshold.

<sup>3</sup> VISIBLE is publicly available at <https://github.com/AstroChem/VISIBLE>

Deprojected and azimuthally averaged radial intensity profiles (Fig. 2) were calculated from the moment-0 maps in Fig. 1 using an inclination of 7° and PA of 155° (Qi et al. 2004; Andrews et al. 2012, 2016). All transitions are centrally peaked, although the beam size is relatively large ( $\sim 50$ –60 AU) compared to the extent of the emission, leaving open the possibility of a ringed morphology at small radii. The transitions all have similar profile shapes, with their relative strengths decreasing with k<sub>a</sub>, although the k<sub>a</sub>=0 and k<sub>a</sub>=1 transitions cross in strength between 55–60 AU. This is just outside the outer edge of the 870μm dust disk, where emission drops sharply around 50 AU (Andrews et al. 2016), suggesting that changes in the disk physical structure at these radii may be affecting either the CH<sub>3</sub>CN vertical abundance distribution or excitation conditions.

We extracted spectra (Fig. 3) of each transition using an elliptical mask 3''.5 in diameter. This corresponds to a radial extent of  $\sim 105$  AU and encapsulates all emission, given the radial profiles in Fig. 2. Flux measurements, listed in Table 1, were then made by integrating these spectra between 2.1 and 3.7 km s<sup>-1</sup>. Uncertainty on each flux measurement was determined through bootstrapping, repeating the integration 10,000 times on an identical number of randomly-selected nearby emission-free channels (sampled with replacement). The standard deviation of these values is reported as the uncertainty on the flux measurement.

## 3. CH<sub>3</sub>CN COLUMN DENSITY AND EXCITATION TEMPERATURE

The k-ladder structure of CH<sub>3</sub>CN's rotational spectrum allows multiple transitions to be observed simultaneously, spanning a wide range of upper state energies. With this large lever arm, the CH<sub>3</sub>CN column density and excitation temperature can be well-constrained through a rotational diagram analysis (e.g., Goldsmith & Langer 1999). We assume LTE excitation, as the critical densities of the J=13–12 and J=12–11 CH<sub>3</sub>CN transitions are  $\sim 2.2 \times 10^6$  and  $\sim 1.7 \times 10^6$  cm<sup>-3</sup>, respectively, at 50K (extrapolated from Shirley 2015). Typical disk gas densities remain above  $1 \times 10^6$  cm<sup>-3</sup>, apart from the upper regions of the disk atmosphere, which we do not expect these observations to probe.

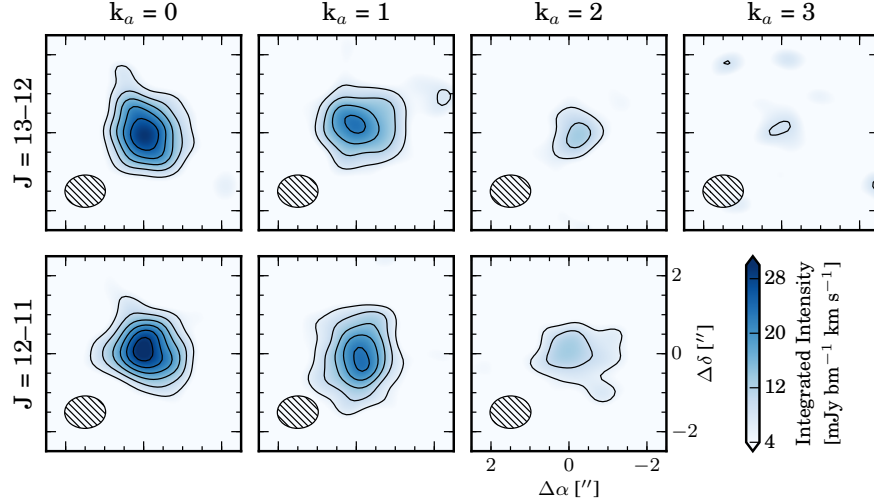


**Figure 1.** Integrated intensity (moment-0) profiles of the observed CH<sub>3</sub>CN transitions, velocity-integrated between 2.1–3.7 km s<sup>-1</sup>. All panels share the same intensity scale. Contours are [3,5,7,...]×σ, where σ=11 mJy km s<sup>-1</sup>. The synthesized beam is shown in the lower left of each panel.

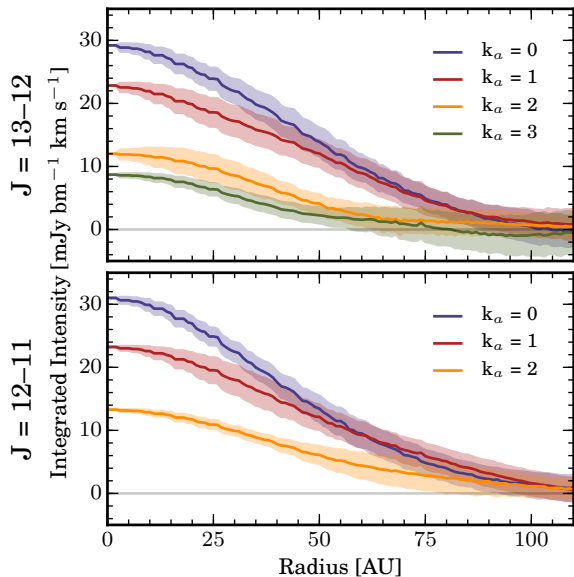


**Figure 2.** Deprojected and azimuthally averaged radial intensity profiles of the observed CH<sub>3</sub>CN transitions. The standard deviations of the mean in each radial bin are used as an estimate of the profile uncertainty and shown as shaded regions.

### 3.1. Disk-averaged analysis

We first calculate a disk-averaged column density and excitation temperature. Under an assumption of optically thin emission, the column density of molecules in the upper state of each transition,  $N_u^{thin}$ , is related to the emission surface brightness,  $I_\nu$  through the equation:

$$I_\nu = \frac{A_{ul} N_u^{thin} h c}{4\pi \Delta V}, \quad (1)$$

where  $A_{ul}$  is the Einstein coefficient and  $\Delta V$  is the linewidth (e.g., Bisschop et al. 2008). The disk-averaged emission intensity  $I_\nu = S_\nu/\Omega$ , where  $S_\nu$  is the flux density and  $\Omega$  is the solid angle subtended by the source.

Substituting for  $I_\nu$  and inverting Eq. 1:

$$N_u^{thin} = \frac{4\pi S_\nu \Delta V}{A_{ul} \Omega h c}. \quad (2)$$

$S_\nu \Delta V$  is the integrated flux density reported for each transition in Table 1, and we use the 3.5'' elliptical mask as an estimate of  $\Omega$ .

Following Gordy & Cook (1984), the upper state level population  $N_u$  can be related to the total column density  $N_T$  by the Boltzmann equation:

$$\frac{N_u}{g_u} = \frac{N_T}{Q(T_{rot})} e^{-E_u/kT_{rot}}, \quad (3)$$

where  $g_u$  is the degeneracy of the upper state level,  $Q$  is the molecular partition function,  $T_{rot}$  is the rotational temperature, and  $E_u$  is the upper state energy. CH<sub>3</sub>CN is a symmetric top with C<sub>3v</sub> symmetry, and the upper state degeneracy  $g_u$  can be written as

$$g_u = g_J g_K g_I \quad (4)$$

where  $g_J = 2J + 1$ ,  $g_K = 1$  for  $K = 0$ , and 2 for  $K \neq 0$ , and  $g_I$  is the reduced nuclear spin degeneracy. For CH<sub>3</sub>CN,  $g_I$  can be defined as

$$g_I = \begin{cases} \frac{1}{3} \left[ 1 + \frac{2}{(2I+1)^2} \right], & \text{for } K = 0, 3, 6, \dots \\ \frac{1}{3} \left[ 1 - \frac{2}{(2I+1)^2} \right], & \text{for } K \text{ not divisible by 3} \end{cases} \quad (5)$$

The partition function  $Q$  can be approximated for a molecule with C<sub>3v</sub> symmetry as

$$Q(T_{rot}) = \left( \frac{5.34 \times 10^6}{\sigma} \right) \left( \frac{T_{rot}^3}{B^2 A} \right)^{1/2}, \quad (6)$$

where  $\sigma$  is a unitless symmetry parameter, equal to 3 for a molecule with C<sub>3v</sub> symmetry, and A and B are the molecular rotational constants. Values for these rotational constants and all other spectral line data were taken from the Spectral Line Atlas of Interstellar Molecules (SLAIM)<sup>4</sup> (F.J. Lovas, private communica-

<sup>4</sup> Available at <http://www.splatalogue.net>.

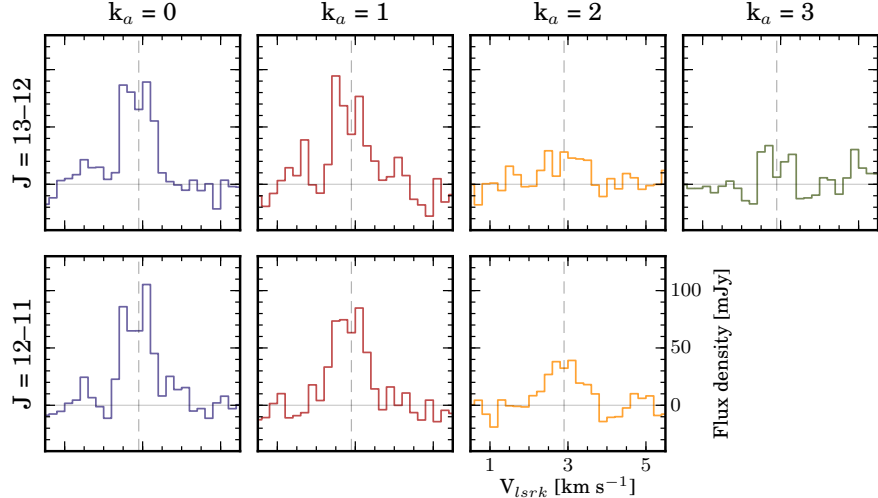


**Figure 3.** Spectra of the observed CH<sub>3</sub>CN transitions, extracted with an elliptical aperture mask 3.''5 in diameter, large enough to cover all CH<sub>3</sub>CN emission.

tion, Remijan et al. 2007).

In a conventional rotational diagram analysis (e.g., Goldsmith & Langer 1999), taking the logarithm of Eq. 3 allows for a linear least squares regression:

$$\ln \frac{N_u}{g_u} = \ln N_T - \ln Q(T_{rot}) - \frac{E_u}{kT_{rot}}. \quad (7)$$

If the level populations,  $N_u/g_u$ , are semi-log plotted against the upper state energies,  $E_u$ , then the rotational temperature,  $T_{rot}$ , and total column density,  $N_T$ , can be derived from the best fit slope and intercept, respectively. Under the assumption of optically thin emission,  $N_u^{thin} = N_u$  and Eq. 2 can be used to calculate  $N_u/g_u$ . The optical depth of the observed CH<sub>3</sub>CN transitions is unknown *a priori*, however. In the case that the optical depth  $\tau \ll 1$ , an optical depth correction factor  $C_\tau$  must be applied:

$$C_\tau = \frac{\tau}{1 - e^{-\tau}}, \quad (8)$$

and thus the true level populations become

$$N_u = N_u^{thin} C_\tau, \quad (9)$$

such that Eq. 7 is rewritten as

$$\ln \frac{N_u}{g_u} + \ln C_\tau = \ln N_T - \ln Q(T_{rot}) - \frac{E_u}{kT_{rot}}. \quad (10)$$

The optical depths of individual transitions are often directly determined through hyperfine ratios or observations of isotopomers, but can also be related back to the upper state level populations:

$$\tau_{ul} = \frac{A_{ul} c^3}{8\pi\nu^3 \Delta V} N_u (e^{h\nu/kT_{rot}} - 1). \quad (11)$$

$C_\tau$  can therefore be written as a function of  $N_u$  and substituted into Eq. 10 to construct a likelihood function  $L(N_u, T_{rot})$ .

Given this likelihood function, we use the affine-invariant MCMC sampler package `emcee` to sample the posterior distributions of both  $N_u$  and  $T_{rot}$ . Random draws from these posteriors are plotted in blue in Fig. 4, with  $\tau$  corrected values of  $N_u/g_u$  plotted

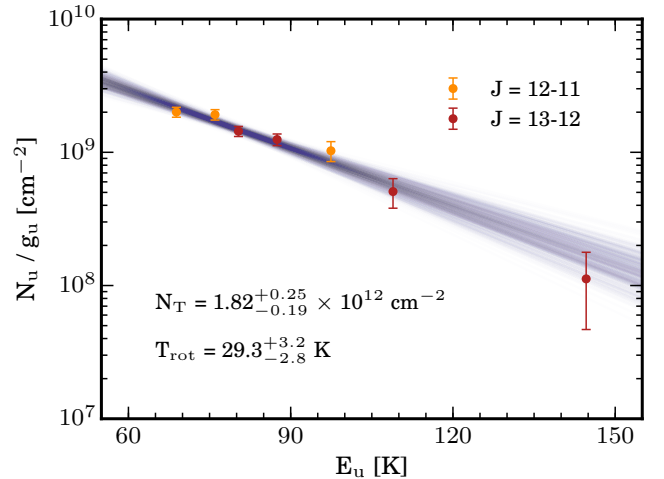


**Figure 4.** CH<sub>3</sub>CN rotational diagram, constructed using disk averaged intensities. J=12-11 and J=13-12 transitions are shown in orange and red, respectively. Random draws from the fit posteriors are plotted in blue.

against  $E_u$ . We find a disk-averaged column density of  $N_T = 1.82^{+0.25}_{-0.19} \times 10^{12} \text{ cm}^{-2}$  and a rotational temperature of  $T_{rot} = 29.3^{+3.2}_{-2.8} \text{ K}$ , where parameters and uncertainties are listed as the 50th, 16th, and 84th percentiles from the marginalized posterior distributions, respectively. Corresponding values of  $\tau$  range between 0.002–0.012, confirming that these transitions of CH<sub>3</sub>CN are optically thin. These values show a good fit to both the complete dataset as well as the individual J=12-11 and J=13-12 k-ladders (shown in orange and red, respectively).

### 3.2. Radially resolved analysis

As the observed CH<sub>3</sub>CN transitions are strongly detected and moderately resolved,  $N_T$  and  $T_{rot}$  can be further constrained as a function of radius. We repeat the rotational diagram analysis previously described, but now use intensities from the radial profiles of each transition from Fig. 2 rather than disk-averaged intensities. Posterior distributions for  $N_T$  and  $T_{rot}$  are calculated at intervals of 1 AU and are plotted in Fig. 5. The rotational diagrams (not shown) remain log-linear and

well-behaved out to  $\sim 70$  AU but become non-linear exterior to this distance, leading to the large uncertainties in  $T_{\text{rot}}$ .

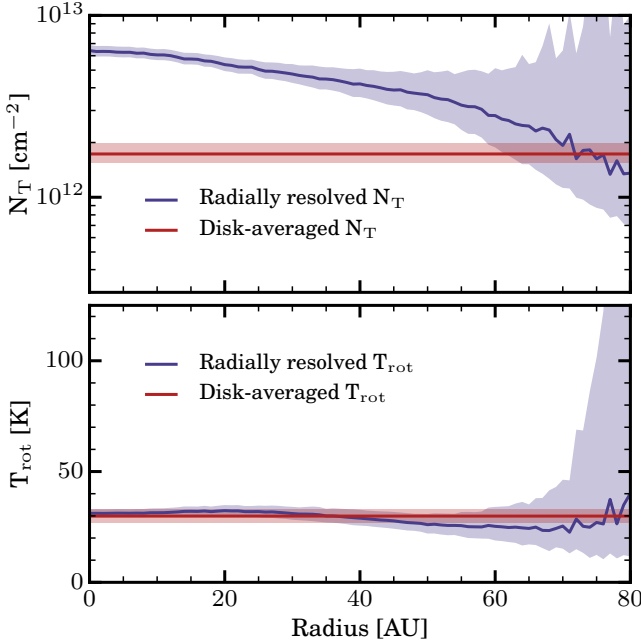


**Figure 5.** Radial profiles of the fit  $\text{CH}_3\text{CN}$  column density (upper panel) and rotational temperature (lower panel). Best fit values and  $1\sigma$  uncertainties are plotted in blue for the radially resolved analysis and in red for the disk-averaged analysis.

$N_T$  decreases with radius, roughly as a power-law for the majority of the disk, and ranges between  $7-1 \times 10^{12} \text{ cm}^{-2}$ . This is consistent with the disk-averaged column density of  $N_T = 1.82^{+0.25}_{-0.19} \times 10^{12} \text{ cm}^{-2}$ , which is overplotted in red in Fig. 5. As the majority of the emission (and therefore molecular column) is concentrated in the inner regions of the disk, the disk-averaged column density is significantly diluted and therefore biased towards the low end of the radially resolved column density range.  $T_{\text{rot}}$  has a relatively flat radial profile, ranging between 30–33 K interior to 40 AU and dipping to  $\sim 25$  K exterior to 40 AU. These values are roughly consistent with the disk-averaged rotation temperature,  $T_{\text{rot}} = 29.3^{+3.2}_{-2.8}$  K.

### 3.3. Comparison to chemical models

We compare the empirical constraints derived in §3.1 and §3.2 to the predictions of a time-dependent chemical model (Fogel et al. 2011; Cleeves et al. 2014) after 10 Myr of chemical evolution. The assumed density and temperature structures of the TW Hya disk were taken from Cleeves et al. (2015) and are shown in Fig. 6, panels a,b. The initial chemical abundances of the model, listed in Table 2, are based on values from Cleeves et al. (2015), updated to have a CO depletion of 20× and an  $\text{H}_2\text{O}$  depletion of 100×. No  $\text{CH}_3\text{CN}$  is included in the initial abundances, and thus all  $\text{CH}_3\text{CN}$  in the model is produced *in situ*. The FUV and X-ray radiation fields within the disk (Fig. 6, panels e,f) were calculated using the Monte Carlo code and cross sections

from Bethell & Bergin (2011), the observed TW Hya FUV spectrum Herczeg et al. (2002, 2004), and a best-fit X-ray model for TW Hya from Cleeves et al. (2015). A reduced cosmic ray ionization rate was assumed (e.g.,  $\zeta_{\text{CR}} \sim (3-7) \times 10^{-17} \text{ s}^{-1}$ , Cleeves et al. 2015).

**Table 2**  
Chemical model initial abundances

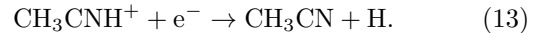
Species	Abundance <sup>a</sup>	Species	Abundance <sup>a</sup>
$\text{H}_2$	$5.00 \times 10^{-1}$	$\text{He}$	$1.40 \times 10^{-1}$
$\text{N}_2$	$3.75 \times 10^{-5}$	$\text{CO}$	$7.00 \times 10^{-6}$
$\text{H}_2\text{O(gr)}$	$2.50 \times 10^{-6}$	$\text{H}_3^+$	$1.00 \times 10^{-8}$
$\text{HCO}^+$	$9.00 \times 10^{-9}$	$\text{C}_2\text{H}$	$8.00 \times 10^{-9}$
$\text{CS}$	$5.00 \times 10^{-9}$	$\text{SO}$	$4.00 \times 10^{-9}$
$\text{C}^+$	$1.00 \times 10^{-9}$	$\text{Si}^+$	$1.00 \times 10^{-11}$
$\text{Mg}^+$	$1.00 \times 10^{-11}$	$\text{Fe}^+$	$1.00 \times 10^{-11}$

<sup>a</sup> Abundances are relative to the proton density  $n_p = 2n_{\text{H}_2}$ .

The chemical reaction network contained a total of 5970 reactions and 600 species. Within this network, three reactions are primarily responsible for the formation of  $\text{CH}_3\text{CN}$  (Walsh et al. 2014; Wakelam et al. 2015). In the gas phase, formation occurs through the radical-neutral reaction (Herbst 1985)



followed by dissociative recombination (Loison et al. 2014)



On grain surfaces, there are two viable formation pathways: (1) sequential hydrogenation of  $\text{C}_2\text{N}$  or (2) a neutral-neutral reaction between  $\text{CH}_3$  and  $\text{CN}$  (Wakelam et al. 2006; Walsh et al. 2014). Destruction pathways for  $\text{CH}_3\text{CN}$  include UV photodissociation into  $\text{CH}_3$  +  $\text{CN}$  and reactions with  $\text{C}^+$ .

To isolate the respective contributions of gas phase and grain-surface formation mechanisms, we ran the chemical model twice, once with grain-surface reactions turned on and once with them turned off. Fig. 6 shows the resultant gas phase  $\text{CH}_3\text{CN}$  abundance profiles (panels b,c). Both gas phase and grain-surface reactions provide significant contributions to the total  $\text{CH}_3\text{CN}$  reservoir, but form distinct vertical layers. Gas phase reactions produce  $\text{CH}_3\text{CN}$  in a banded layer at  $z/r \sim 0.5$ , where the gas temperature is  $\sim 40$ –50 K. The upper boundary of this layer sits along the FUV  $\tau=1$  surface, and is primarily set by the UV photo-dissociation of  $\text{CH}_3\text{CN}$ . The lower boundary of the layer is set by high FUV and X-ray optical depths, where the reactant  $\text{C}_3\text{H}^+$  is not formed in appreciable quantities. The gas phase contribution is centrally peaked, with column densities falling several orders of magnitude by 50 AU. In contrast, grain-surface reactions produce a band of  $\text{CH}_3\text{CN}$  in the gas phase at  $z/r \sim 0.3$  ( $T_{\text{gas}} \sim 30$  K) which is sustained out to larger radii. Grain-surface formation is dominated in the model by sequential  $\text{C}_2\text{N}$  hydrogenation, with an upper boundary set by the freeze-out of reactants and a lower boundary set by high optical depths limiting photodesorption of  $\text{CH}_3\text{CN}$  off the grain surfaces.

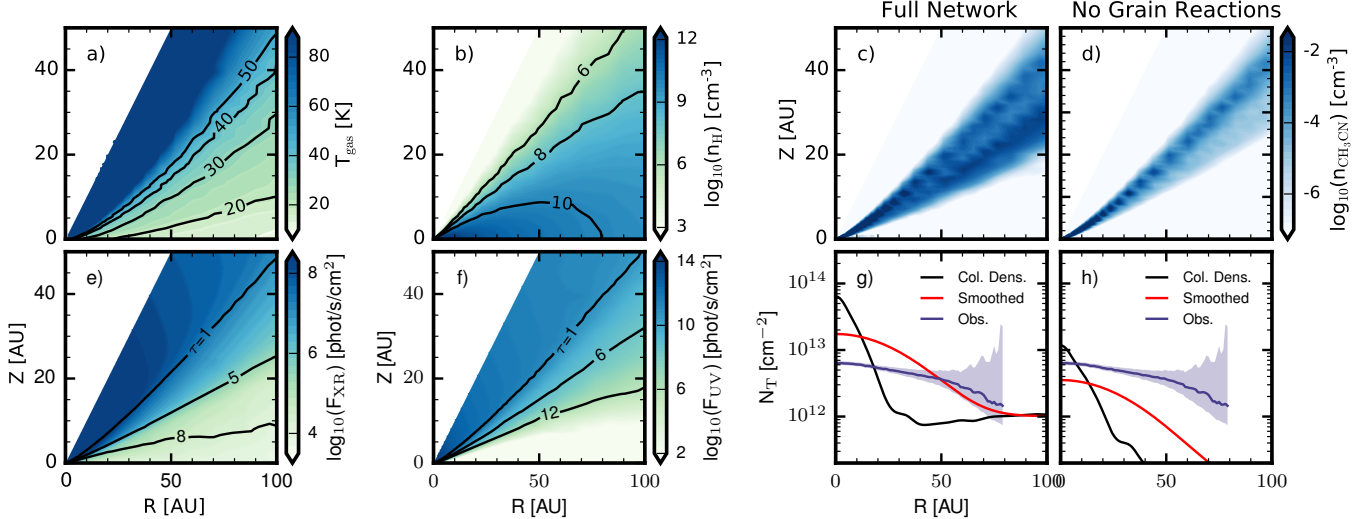


**Figure 6.** Chemical modelling summary. *Panels (a,b)*: Disk temperature and density structures, respectively taken from (Cleeves et al. 2015). *Panels (c,d)*:  $\text{CH}_3\text{CN}$  gas-phase abundance in model with grain-surface reactions turned on and off, respectively. *Panels (e,f)*: X-ray and FUV radiation fields, respectively, with optical depths overplotted as contours. *Panels (g,h)*:  $\text{CH}_3\text{CN}$  gas-phase column densities for the abundance profiles shown in panels c and d, respectively. Column density profiles smoothed with a Gaussian the size of the synthesized beam are overplotted in red, and the observed column density profile from Fig. 5 is overplotted in blue out to 80 AU.

These abundance profiles were vertically integrated to calculate column density profiles (Fig. 6 panels e,f). The model column density profiles, shown in black, were convolved with a Gaussian kernel (FWHM=60 AU) to produce the smoothed profiles shown in red, simulating the effect of beam convolution in our observations. Grain-surface contributions in the full network model increase the integrated column density by a factor of 4–10× across the disk. Gas phase reactions alone are insufficient to reproduce the observed column densities in Fig. 4 (between  $10^{13}$ – $10^{12}$  cm $^{-2}$ ) out to large radii, while the inclusion of grain-surface reactions produces ample column to reproduce the observations.

To compare better compare this model with the observations, we calculated simulated emission profiles of all observed  $\text{CH}_3\text{CN}$  transitions using the radiative transfer code RADMC-3D (Dullemond et al. 2012). A distance of 59.5 pc, inclination of 7°, PA of 155°, and stellar mass of 0.8  $M_\odot$  (to determine line broadening) were assumed for the radiative transfer (Kastner et al. 1997; Qi et al. 2004; Andrews et al. 2012, 2016). Simulated ALMA observations were then calculated for each transition using the `vis_sample` package (Loomis et al. subm.) and the antenna configuration of the original observations. From these simulated observations, we extracted the deprojected and azimuthally-averaged radial intensity profiles shown in Fig. 7. These profiles are very similar to the observed radial profiles in Fig. 7, with fluxes for six of the seven transitions matching within 30% and emission reaching unobservable levels by 100 AU. The  $13_3-12_3$  transition is the only transition which does not match as well, with the model predicting almost double the observed emission. Possible reasons for this discrepancy are discussed in §4.1.

We additionally repeated the analysis described in §3.1 on the model observations and calculated a disk-averaged rotational temperature and column density (Fig. 8). The calculated column density of  $N_T=1.46_{-0.11}^{+0.15} \times 10^{12}$  cm $^{-2}$

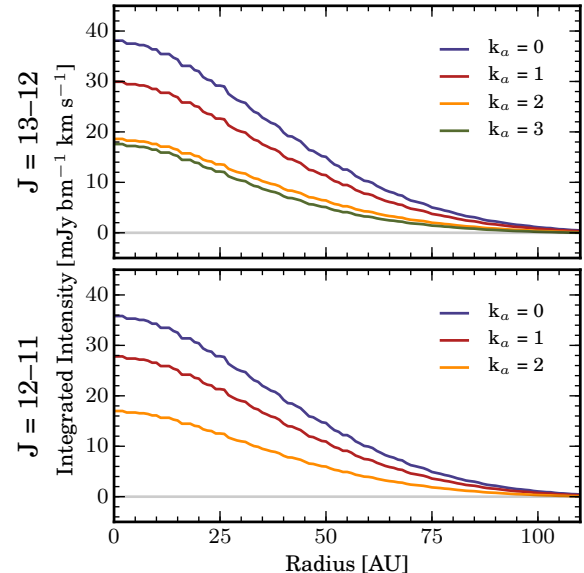


**Figure 7.** Deprojected and azimuthally averaged radial intensity profiles of the modeled  $\text{CH}_3\text{CN}$  transitions.

is within 25% of the observed column density of  $N_T=1.82_{-0.19}^{+0.25} \times 10^{12}$  cm $^{-2}$ , but the calculated rotational temperature of  $T_{rot}=37.0_{-3.7}^{+4.2}$  K is somewhat higher than the observed rotational temperature of  $T_{rot}=29.3_{-2.8}^{+3.2}$  K. These differences are further discussed in §4.1.

## 4. DISCUSSION

### 4.1. $\text{CH}_3\text{CN}$ abundance structure and formation chemistry

The results of our rotational diagram analysis suggest that  $\text{CH}_3\text{CN}$  in TW Hya emits from a banded layer in the disk at a relatively constant temperature of  $\sim 30$  K, roughly corresponding to  $z/r \sim 0.3$ . These first observational constraints on the vertical distribution of  $\text{CH}_3\text{CN}$

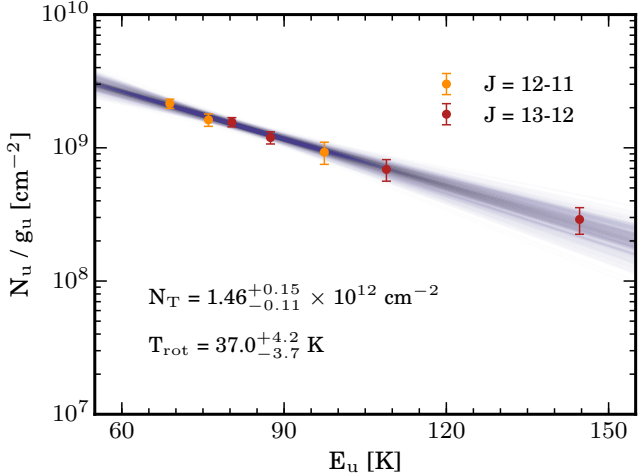


**Figure 8.** Modeled CH<sub>3</sub>CN rotational diagram, constructed using disk averaged intensities from simobserved models. J=12–11 and J=13–12 transitions are shown in orange and red, respectively. Random draws from the fit posteriors are plotted in blue.

are in good agreement with predictions of a banded layer from the chemical models presented in Öberg et al. (2015). The layer found in Öberg et al. (2015) was warmer ( $\sim 50$  K) than the  $\sim 30$  K we observe, but this is likely due to the orders of magnitude higher UV flux that MWC 480 is subjected to, compared to TW Hya (e.g., D'Alessio et al. 2004). Similarly, we find that our observed radial column density profile is in good qualitative agreement with the predictions of Walsh et al. (2014) and the observational results of Öberg et al. (2015), which both found a column density profile that ranged between  $\sim 10^{12}$ – $10^{13}$  cm $^{-2}$  and monotonically decreased with radius. In both our observations and those of Öberg et al. (2015), however, relatively low spatial resolution precludes a more detailed analysis of the radial CH<sub>3</sub>CN distribution.

We attempt to gain an intuition for the dominant CH<sub>3</sub>CN formation pathway by comparing these observational results with two chemical models, with and without grain-surface chemistry. The full chemical network, which we note has not been adjusted in any manner to better match the data, predicts emission which is in remarkably good agreement with our observations, reproducing fluxes for six of seven transitions to within 30% (Fig. 7). The model with no grain-surface reactions underpredicts our measured fluxes by over an order of magnitude, suggesting that grain-surface formation of CH<sub>3</sub>CN (which also dominates the full network) is the main *in situ* formation pathway. This is further supported by our observed temperature layer ( $\sim 30$  K, z/r $\sim 0.3$ ) being well matched to the grain-surface formation layer shown in Fig. 6, panel c. Dominant grain-surface formation which is able to reproduce observed CH<sub>3</sub>CN fluxes solely through *in situ* formation additionally matches predictions from Öberg et al. (2015), where a high CH<sub>3</sub>CN/HCN ratio compared to protostellar regions (e.g., van Dishoeck et al. 1995) was invoked to suggest limited CH<sub>3</sub>CN contributions from inheritance alone.

Although the full network model predicts adequate

integrated fluxes, several key differences in the radial and vertical CH<sub>3</sub>CN distributions exist between the model and our observational results. First, the model column density radially profile is more centrally peaked (even after beam convolution) than the observed column density profile (Fig. 6). Second, the simulated emission profile of the 13<sub>3</sub>–12<sub>3</sub> transition (Fig. 7) is almost double the brightness of the observed emission (Fig. 2). Third, although the best-fit disk-averaged column density from the simulated model observations ( $N_T=1.46^{+0.15}_{-0.11} \times 10^{12}$  cm $^{-2}$ ) is within 25% of the observed column density ( $N_T=1.82^{+0.25}_{-0.19} \times 10^{12}$  cm $^{-2}$ ), the model disk-averaged rotational temperature ( $T_{rot}=37.0^{+4.2}_{-3.7}$  K) is considerably higher than the observed rotational temperature ( $T_{rot}=29.3^{+3.2}_{-2.8}$  K).

These three differences are inherently linked; a more centrally peaked column density results in more emission at small radii, where the gas temperature is higher for a given z/r. As the 13<sub>3</sub>–12<sub>3</sub> transition has the highest upper state energy, its flux is the most sensitive to this temperature. A number of phenomena therefore could possibly explain these discrepancies. First, a central depletion in the CH<sub>3</sub>CN emission cannot be ruled out by our observations, given their relatively low spatial resolution. By stacking the observations and examining the resultant channel maps, we are able to constrain the possible radial extent of such a feature to be less than 16 AU (see Appendix A). Second, the gas-phase formation of CH<sub>3</sub>CN or its grain-surface precursor C<sub>2</sub>N may be too efficient in the chemical model. This could result from uncertain reaction rates or a different C/O ratio than the model assumes, given our assumptions on both CO and H<sub>2</sub>O depletion. Formation of cyanides such as CH<sub>3</sub>CN is sensitive to carbon and oxygen abundances, with depleted abundances resulting in more efficient cyanide formation (Du et al. 2015). Finally, the temperature of the CH<sub>3</sub>CN emission is likely sensitive to our assumptions on the TW Hya FUV and X-ray radiation fields, as the boundaries of the CH<sub>3</sub>CN layer are directly linked to the optical depths of the radiation fields, as discussed in §3.3. Future model refinement to better fit CH<sub>3</sub>CN and address these discrepancies may be possible by additionally using high resolution observations of smaller molecules such as HCN and their isotopologues to anchor the initial conditions and physical characteristics of the model.

#### 4.2. Implications for cometary CH<sub>3</sub>CN abundances

Interpreting the implications of these results for the chemical composition of forming exocomets requires extrapolation to the midplane, as our gas-phase observations probe a higher layer at z/r $\sim 0.3$ . Additionally, the bulk composition of forming comets and planetesimals will be primarily set by grain-surface chemical abundances, rather than gas-phase abundances. Fig. 9 panels a,b show the grain-surface abundances of CH<sub>3</sub>CN in our chemical models, with grain-surface chemistry turned on and off, respectively. Although no CH<sub>3</sub>CN is formed on grain-surfaces in the latter model, freeze-out still results in a non-negligible CH<sub>3</sub>CN grain-surface abundance. To compare these grain-surface abundances to measured cometary CH<sub>3</sub>CN abundances in the Solar System ( $\sim 10^{-4}$ , e.g., Mumma & Charnley 2011), panels

c,d of Fig. 9 show  $\text{CH}_3\text{CN}(\text{gr})/\text{H}_2\text{O}(\text{gr})$  abundance ratios across the disk. As all  $\text{CH}_3\text{CN}$  in the models is formed *in situ*, with no inheritance, these values represent a lower bound on the possible  $\text{CH}_3\text{CN}(\text{gr})/\text{H}_2\text{O}(\text{gr})$  ratios. Gas-phase reactions alone (panel d) are clearly insufficient to reproduce cometary abundances of  $\text{CH}_3\text{CN}$ , while the incorporation of grain-surface reactions (panel c) produces abundances close to cometary values in the comet forming regions of the disk ( $\sim 10\text{--}30$  AU), consistent with the results of Walsh et al. (2014).

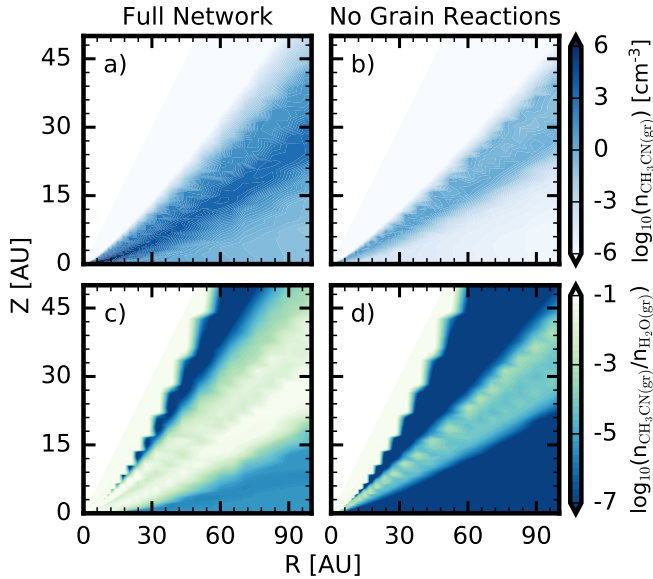


**Figure 9.** Panels (a,b):  $\text{CH}_3\text{CN}$  abundances in the solid-phase on grain-surfaces, calculated in chemical models with grain-surface reactions turned on and off, respectively. Panels (c,d):  $\text{CH}_3\text{CN}(\text{gr})/\text{H}_2\text{O}(\text{gr})$  abundance ratios, calculated from the abundance profiles shown in panels a and b. Note that all  $\text{CH}_3\text{CN}$  in the models is formed *in situ*, while initial abundances of  $\text{H}_2\text{O}$  are inherited from the protostellar phase (see Table 2).

Fig. 10 plots  $\text{CH}_3\text{CN}(\text{gr})/\text{H}_2\text{O}(\text{gr})$  ratios at a variety of  $z/r$  cuts through the disk, comparing these values to the range of known cometary  $\text{CH}_3\text{CN}(\text{gr})/\text{H}_2\text{O}(\text{gr})$  ratios ( $7 \times 10^{-5}\text{--}3 \times 10^{-4}$ , e.g., Mumma & Charnley 2011). *In situ* formation in the comet forming zone ( $10\text{--}30$  AU) is insufficient to produce cometary abundances of  $\text{CH}_3\text{CN}$  at the midplane, but can easily yield these abundances at slightly higher disk layers. Thus a detailed understanding of the coupling between chemistry and vertical motion of material within the disk (e.g., Semenov & Wiebe 2011) will be necessary to determine if  $\text{CH}_3\text{CN}$  produced higher in the disk can be efficiently transported to the midplane for incorporation into comets. In particular, analysis of cometary inheritance of  $\text{CH}_3\text{CN}$  will require chemical modeling which incorporates both dust settling and turbulent diffusion, as these phenomena have pronounced effects on  $\text{CH}_3\text{CN}$  abundance distributions and the coupling between gas-phase and grain surface abundances (e.g., Semenov & Wiebe 2011; Öberg et al. 2015).

## 5. SUMMARY

In summary, we have detected emission from seven transitions of  $\text{CH}_3\text{CN}$  toward TW Hya. A disk-

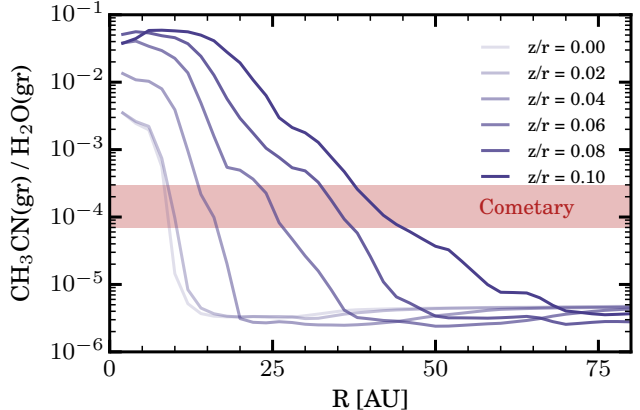


**Figure 10.**  $\text{CH}_3\text{CN}(\text{gr})/\text{H}_2\text{O}(\text{gr})$  abundance ratios from Fig. 9, panel c (full chemical network), taken at different  $z/r$  slices.

averaged rotational analysis finds a column density of  $N_T = 1.82^{+0.25}_{-0.19} \times 10^{12} \text{ cm}^{-2}$  and a rotational temperature of  $T_{rot} = 29.3^{+3.2}_{-2.8} \text{ K}$ , and a radially resolved analysis shows this temperature to be flat across the disk. We interpret these results to suggest that  $\text{CH}_3\text{CN}$  emission originates from a banded layer at  $z/r \sim 0.3$ . Comparing these observations with the results of a disk chemistry model, we determine that grain-surface reactions likely dominate  $\text{CH}_3\text{CN}$  formation. *In situ* formation in the model is sufficient to explain observed  $\text{CH}_3\text{CN}$  fluxes, although further model refinement is necessary to accurately reproduce  $\text{CH}_3\text{CN}$  radial and vertical abundance profiles. Finally, we examine the  $\text{CH}_3\text{CN}(\text{gr})/\text{H}_2\text{O}(\text{gr})$  ratio predicted by our model and find that cometary abundances of  $\text{CH}_3\text{CN}$  are not present in the disk midplane, but are found in slightly higher disk layers, suggesting that inclusion of dust settling or turbulent mixing may be necessary to replicate cometary  $\text{CH}_3\text{CN}$  abundances in the midplane.

RAL gratefully acknowledges funding from NRAO Student Observing Support. KIÖ acknowledges funding from the Simons Collaboration on the Origins of Life (SCOL), the Alfred P. Sloan Foundation, and the David and Lucile Packard Foundation. The National Radio Astronomy Observatory is a facility of the National Science Foundation operated under cooperative agreement by Associated Universities, Inc. This paper makes use of the following ALMA data: ADS/JAO.ALMA #2016.1.01046.S. ALMA is a partnership of ESO (representing its member states), NSF (USA) and NINS (Japan), together with NRC (Canada) and NSC and ASIAA (Taiwan), in cooperation with the Republic of Chile. The Joint ALMA Observatory is operated by ESO, AUI/NRAO and NAOJ.

## REFERENCES

- Andrews, S. M., Wilner, D. J., Hughes, A. M., Qi, C., Rosenfeld, K. A., Öberg, K. I., Birnstiel, T., Espaillat, C., Cieza, L. A., Williams, J. P., Lin, S.-Y., & Ho, P. T. P. 2012, ApJ, 744, 162
- Andrews, S. M., Wilner, D. J., Zhu, Z., Birnstiel, T., Carpenter, J. M., Pérez, L. M., Bai, X.-N., Öberg, K. I., Hughes, A. M., Isella, A., & Ricci, L. 2016, ApJ, 820, L40

- Bergin, E. A., Cleeves, L. I., Gorti, U., Zhang, K., Blake, G. A., Green, J. D., Andrews, S. M., Evans, II, N. J., Henning, T., Öberg, K., Pontoppidan, K., Qi, C., Salyk, C., & van Dishoeck, E. F. 2013, *Nature*, 493, 644
- Bernstein, M. P., Dworkin, J. P., Sandford, S. A., Cooper, G. W., & Allamandola, L. J. 2002, *Nature*, 416, 401
- Bethell, T. J. & Bergin, E. A. 2011, *ApJ*, 740, 7
- Bisschop, S. E., Jørgensen, J. K., Bourke, T. L., Bottinelli, S., & van Dishoeck, E. F. 2008, *A&A*, 488, 959
- Chapillon, E., Dutrey, A., Guilloteau, S., Piétu, V., Wakelam, V., Hersant, F., Gueth, F., Henning, T., Launhardt, R., Schreyer, K., & Semenov, D. 2012, *ApJ*, 756, 58
- Cleeves, L. I., Bergin, E. A., & Adams, F. C. 2014, *ApJ*, 794, 123
- Cleeves, L. I., Bergin, E. A., Qi, C., Adams, F. C., & Öberg, K. I. 2015, *ApJ*, 799, 204
- Cordiner, M. A., Remijan, A. J., Boissier, J., Milam, S. N., Mumma, M. J., Charnley, S. B., Paganini, L., Villanueva, G., Bockelée-Morvan, D., Kuan, Y.-J., Chuang, Y.-L., Lis, D. C., Biver, N., Crovisier, J., Minniti, D., & Coulson, I. M. 2014, *ApJ*, 792, L2
- D'Alessio, P., Calvet, N., Hartmann, L., Muñoz, J., & Sitko, M. 2004, in *IAU Symposium*, Vol. 221, Star Formation at High Angular Resolution, ed. M. G. Burton, R. Jayawardhana, & T. L. Bourke, 403
- Du, F., Bergin, E. A., & Hogerheijde, M. R. 2015, *ApJ*, 807, L32
- Dullemond, C. P., Juhasz, A., Pohl, A., Sereshti, F., Shetty, R., Peters, T., Commercon, B., & Flock, M. 2012, RADMC-3D: A multi-purpose radiative transfer tool, Astrophysics Source Code Library
- Dutrey, A., Guilloteau, S., & Guelin, M. 1997, *A&A*, 317, L55
- Fogel, J. K. J., Bethell, T. J., Bergin, E. A., Calvet, N., & Semenov, D. 2011, *ApJ*, 726, 29
- Goldsmith, P. F. & Langer, W. D. 1999, *ApJ*, 517, 209
- Gordy, W. & Cook, R. L. 1984, Microwave molecular spectra, [3rd ed.] edn. (New York : Wiley), "A Wiley-Interscience Publication."
- Herbst, E. 1985, *Astrophysical Journal*, 291, 226
- Herczeg, G. J., Linsky, J. L., Valenti, J. A., Johns-Krull, C. M., & Wood, B. E. 2002, *ApJ*, 572, 310
- Herczeg, G. J., Wood, B. E., Linsky, J. L., Valenti, J. A., & Johns-Krull, C. M. 2004, *ApJ*, 607, 369
- Jørgensen, J. K., van der Wiel, M. H. D., Coutens, A., Lykke, J. M., Müller, H. S. P., van Dishoeck, E. F., Calcutt, H., Bjerkeli, P., Bourke, T. L., Drozdovskaya, M. N., Favre, C., Fayolle, E. C., Garrod, R. T., Jacobsen, S. K., Öberg, K. I., Persson, M. V., & Wampfler, S. F. 2016, *A&A*, 595, A117
- Kastner, J. H., Zuckerman, B., Weintraub, D. A., & Forveille, T. 1997, *Science*, 277, 67
- Le Roy, L., Altweig, K., Balsiger, H., Berthelier, J.-J., Bieler, A., Briois, C., Calmonte, U., Combi, M. R., De Keyser, J., Dhooghe, F., Fiethe, B., Fuselier, S. A., Gasc, S., Gombosi, T. I., Hässig, M., Jäckel, A., Rubin, M., & Tzou, C.-Y. 2015, *A&A*, 583, A1
- Loison, J.-C., Wakelam, V., & Hickson, K. 2014, *Monthly Notices of The Royal Astronomical Society*, 443, 398
- Mumma, M. J. & Charnley, S. B. 2011, *ARA&A*, 49, 471
- Öberg, K. I., Guzmán, V. V., Furuya, K., Qi, C., Aikawa, Y., Andrews, S. M., Loomis, R., & Wilner, D. J. 2015, *Nature*, 520, 198
- Patel, B. H., Percivalle, C., Ritson, D. J., D., & Sutherland, J. D. 2015, *Nat Chem*, 7, 301, article
- Pownert, M. W., Gerland, B., & Sutherland, J. D. 2009, *Nature*, 459, 239
- Pownert, M. W., Sutherland, J. D., & Szostak, J. W. 2010, *Journal of the American Chemical Society*, 132, 16677, PMID: 21043502
- Qi, C., Ho, P. T. P., Wilner, D. J., Takakuwa, S., Hirano, N., Ohashi, N., Bourke, T. L., Zhang, Q., Blake, G. A., Hogerheijde, M., Saito, M., Choi, M., & Yang, J. 2004, *ApJ*, 616, L11
- Qi, C., Wilner, D. J., Calvet, N., Bourke, T. L., Blake, G. A., Hogerheijde, M. R., Ho, P. T. P., & Bergin, E. 2006, *ApJ*, 636, L157
- Remijan, A. J., Markwick-Kemper, A., & ALMA Working Group on Spectral Line Frequencies. 2007, in *Bulletin of the American Astronomical Society*, Vol. 39, American Astronomical Society Meeting Abstracts, 963
- Sakai, N., Sakai, T., Hirota, T., Watanabe, Y., Ceccarelli, C., Kahane, C., Bottinelli, S., Caux, E., Demyk, K., Vastel, C., Coutens, A., Taquet, V., Ohashi, N., Takakuwa, S., Yen, H.-W., Aikawa, Y., & Yamamoto, S. 2014, *Nature*, 507, 78
- Semenov, D. & Wiebe, D. 2011, *ApJS*, 196, 25
- Shirley, Y. L. 2015, *PASP*, 127, 299
- van Dishoeck, E. F., Blake, G. A., Jansen, D. J., & Groesbeck, T. D. 1995, *ApJ*, 447, 760
- van Zadelhoff, G.-J., van Dishoeck, E. F., Thi, W.-F., & Blake, G. A. 2001, *A&A*, 377, 566
- Wakelam, V., Herbst, E., & Selsis, F. 2006, *A&A*, 451, 551
- Wakelam, V., Loison, J.-C., Herbst, E., Pavone, B., Bergeat, A., Béroff, K., Chabot, M., Faure, A., Galli, D., Geppert, W. D., Gerlich, D., Gratier, P., Harada, N., Hickson, K. M., Honvárt, P., Klippenstein, S. J., Le Picard, S. D., Nyman, G., Ruaud, M., Schlemmer, S., Sims, I. R., Talbi, D., Tennyson, J., & Wester, R. 2015, *ApJS*, 217, 20
- Walsh, C., Millar, T. J., Nomura, H., Herbst, E., Widicus Weaver, S., Aikawa, Y., Laas, J. C., & Vasyunin, A. I. 2014, *A&A*, 563, A33

## APPENDIX

A. CH<sub>3</sub>CN CHANNEL MAPS

Channel maps of the observed CH<sub>3</sub>CN transitions are shown in Fig. 11, generated from the image cubes described in §2 at 0.2 km s<sup>-1</sup>. To better investigate the distribution of CH<sub>3</sub>CN at small radii, we additionally stacked the transitions within each k-ladder to improve the signal-to-noise ratio (SNR). The filter responses of each transition were used as an estimate of their inherent SNR, and applied as stacking weights when the measurement sets were combined in the uv-plane. The stacked measurement sets were identically imaged to the individual transitions, and show evidence for emission up to 0.8 km s<sup>-1</sup> from the systemic velocity, corresponding to a radius of ~16 AU, assuming a stellar mass of 0.8 M<sub>⊙</sub> and inclination of 7 degrees. The data are therefore compatible with the presence of a depression in CH<sub>3</sub>CN surface density at small radii, but constrain the size such a feature to be less than 16 AU.

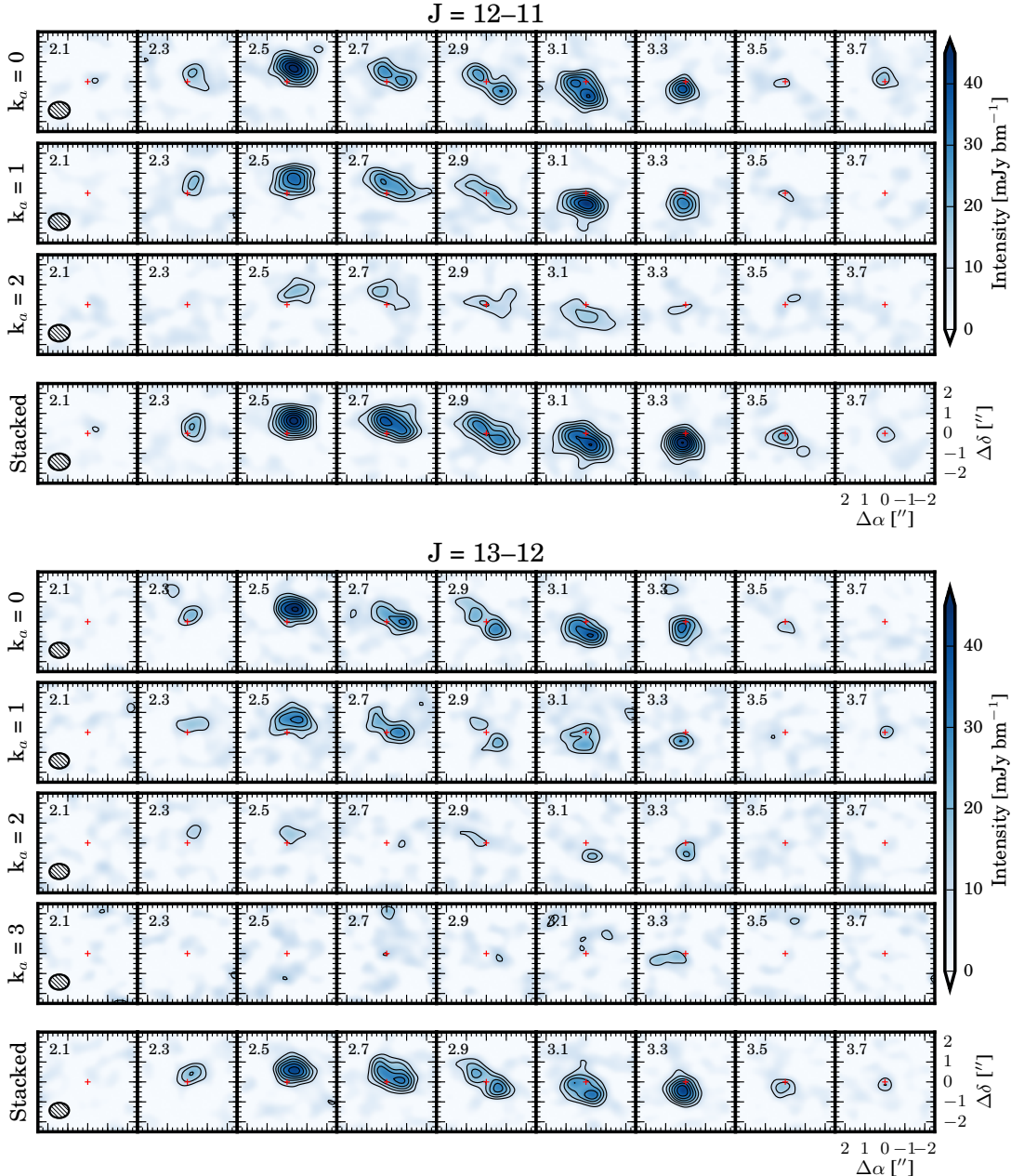


**Figure 11.** Channel maps of the observed CH<sub>3</sub>CN transitions and stacked J=12–11 and J=13–12 k-ladders, with 0.2 km s<sup>-1</sup> channel spacing. All panels share the same intensity scale. Contours are [3,5,7,...] × σ, where σ = 3.2 mJy km s<sup>-1</sup>. The synthesized beam is shown in the left panel of each row.